JOURNAL OF SOLID STATE CHEMISTRY 102, 20–30 (1993)

$Pb_{1-x}Sr_4Fe_2O_{9-\delta}$: A Layered Iron Oxide Intergrowth of 1201- and 0201-Type Structures

S. LUCAS, D. GROULT,* N. NGUYEN, C. MICHEL, M. HERVIEU, AND B. RAVEAU

Laboratoire CRISMAT, URA 1318, associée au CNRS ISMRa, Bd. du Maréchal Juin, 14050 Caen Cedex, France

Received February 1992; accepted May 7, 1992

A new layered iron oxide, $Pb_{1-x}Sr_4Fe_2O_{9-\delta}$, has been isolated for $0 \leq x \leq 0.2$. Its structural model, which corresponds to a regular intergrowth of single $[SrFeO_{3-\delta}]_x$ perovskite layers with single $[SrO]_x$ and double $[(SrO)(Pb_{1-x}O)]_x$ rock salt layers, has been established by high resolution electron microscopy (HREM) and powder XRD. The existence of numerous defects—local variation of the nature of the cations, modulations of the atomic layers, and intergrowth defects interpreted as $[Sr_3Fe_2O_{7-\delta}]_x$ and $[Sr_4Fe_3O_{10-\delta}]$ layers—has been observed by HREM. The existence for Fe(III) of two "5 + 1" coordinations for $x = 0$, and of three coordinations for $x \neq 0$ (two 5 + 1 and one pure pyramidal coordination) has been deduced from Mössbauer spectroscopy measurements.

Introduction

Substitution of iron for copper in high T_c superconducting cuprates has been the purpose of several studies in order to understand the origin of superconductivity and to investigate the relationships between structure and superconductivity in these materials. The replacement of copper by iron in the 123 structure (*1–6*) has shown the predominant role of the pyramidal copper layers in the superconducting properties of these materials. The synthesis and structural studies of the layered iron oxides $Bi_2Sr_{3-x}Ca_xFe_2O_9$ (*7*) and $Bi_2Sr_4Fe_3O_{12-\delta}$ (*8*), isotypic with the superconductors $Bi_2Sr_2CaCu_2O_8$ and $Bi_2Sr_2Ca_2Cu_3O_{10}$, respectively, have demonstrated that the modulation of the structure of all these phases was not related to superconductivity and was mainly due to the bismuth oxygen layers. Recently several superconducting 1212-type lead cuprates with the general formula $Pb_{1-x}A_xSr_2Y_{1-x}Ca_xCu_2O_{7-\delta}$ (A = Cu, Ca, Sr) were isolated (*9–16*). With the intention of synthesizing isotypic iron layered cuprates, the system Pb–Sr–Fe–O was investigated. We report here on a new layered iron oxide, $Pb_{1-x}Sr_4Fe_2O_{9-\delta}$, whose structure corresponds to an intergrowth of the 0201-La_2CuO_4-type oxide with the 1201-$TlSrLaCuO_5$-type oxide (*17*).

Experimental

Synthesis. The title compounds, corresponding to x values ranging approximately from 0 to 0.2, have been prepared from mix-

* To whom correspondence should be addressed.

0022-4596/93 $5.00

tures of PbO, Fe_2O_3, and $SrCO_3$. For $x \approx 0.2$ the starting materials were mixed in the molar ratio 1 : 1 : 4 while they were mixed in the molar ratio 1.75 : 1 : 4 for $x = 0$.

The mixtures were first heated in air at 900°C for 12 hr in an alumina crucible and quenched to room temperature. At this step of the solid state reaction, the weight loss indicated that besides the loss of CO_2 there was also an uptake of oxygen corresponding to the oxidation of Pb(II) to Pb(IV). This was confirmed by XRD patterns which exhibited indeed the presence of Sr_2PbO_4 mixed with the new oxide described here. Further annealings at 1000°C for 12 hr were then carried out in order to obtain the new compound as a single phase. After each annealing the weight loss was measured and compared to the theoretical one.

X-ray and chemical analyses. The homogeneity of the samples was checked in the course of the reaction by X-ray diffraction using a Philips diffractometer with Cu$K\alpha$ radiation. The chemical analyses of the compounds judged from X-ray analysis as pure phases were carried out by means of a classical oxidometric titration of Pb(IV). The total lead content was determined by electrolysis.

High resolution electron microscopy (HREM) study and crystal structure calculations. HREM investigation was performed by use of a TOPCON 02B electron microscope fitted with a double tilt sample holder ($V = 200$ kV, $C_s = 0.4$ mm). Powder X-ray diffraction data for crystal structure calculations were collected at 300 K by step scanning over an angular range of 5° to 100° in 2θ with an increment of 0.02°. The analysis by the Rietveld method was carried out by means of a DBW 3.2 program (*18*).

Mössbauer spectroscopy and magnetic measurements. The title compounds were characterized by Mössbauer spectroscopy using a constant acceleration spectrometer with a ^{57}Co source in a Rh matrix at 300 K. The magnetic susceptibility was measured with a Faraday balance in the temperature range 4 to 750 K.

Results and Discussion

X-ray structure calculations based on the HREM study. Using two subsequent annealings at 1000°C for 12 hr, a single phase was isolated. The T.G. analysis indicated a significant weight loss with respect to the nominal composition, which was attributed to PbO volatility. The lead analysis, using both electrolysis and oxidometric titrations (Table I), allowed this hypothesis to be confirmed and showed that the total lead amount was tetravalent. Thus, this single phase can be formulated $Pb_{1-x}Sr_2Fe_4O_{9-\delta}$ with $0 \leq x \leq 0.2$.

According to electron diffraction data, the symmetry of the crystals is tetragonal with $a \approx a_p$ (a_p referred to the parameter of the

TABLE I

LEAD CONTENT AND LATTICE PARAMETERS OBSERVED FOR $Pb_{1-x}Sr_4Fe_2O_{9-\delta}$

Molar ratios of starting materials PbO : Fe_2O_3 : $SrCO_3$	Final lead content of the samples		Lattice parameters	
	Oxidometry ±0.05	Electrolysis ±0.03	a (Å)	c (Å)
1 : 1 : 4	0.82	0.78	3.8349(1)	30.664(1)
1.25 : 1 : 4	0.89	0.85	3.8354(1)	30.663(2)
1.50 : 1 : 4	0.94	0.89	3.8385(2)	30.666(2)
1.75 : 1 : 4	1.04	0.98	3.8445(1)	30.670(2)

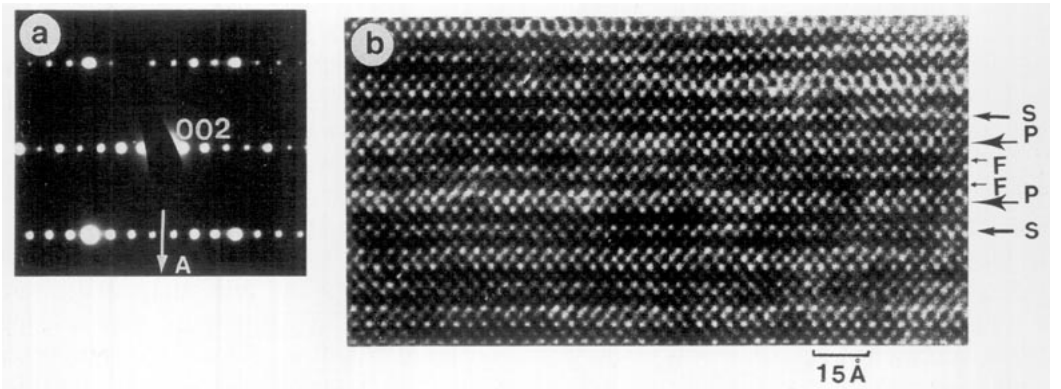

FIG. 1. (a) [100] E.D. pattern of a $Pb_{1-x}Sr_4Fe_2O_{9-\delta}$ sample ($x \approx 0.2$). (b) [100] high resolution of $Pb_{1-x}Sr_4Fe_2O_{9-\delta}$. The contrast consists of a regular alternation of two and three rows of bright dots separated by single rows of weak dots. The first ones are correlated with the strontium–oxygen and lead–oxygen layers, labeled S and P, respectively. The rows of weak dots are correlated with the FeO_2 layers, labeled F.

cubic perovskite cell) and c close to 31 Å. Reflection conditions are hkl, $h + k + l = 2n$, involving an I-type space group. A typical [100] ED pattern is shown in Fig. 1a. On this basis, the X-ray diffraction patterns corresponding to $0 \leq x \leq 0.20$ were indexed (Table I) in this tetragonal cell. The c parameter does not vary significantly with x, whereas the a parameter is more sensitive to the lead content.

The above results suggest that this lead iron oxide is closely related to the superconductive thallium cuprate $TlBa_{2-x}La_{2+x}Cu_2O_{9\pm\delta}$ (*19*), whose structure consists of an intergrowth of single perovskite layers with single $[LaO]_\infty$ and double $[(BaO)(TlO)]_\infty$ rock salt layers. In order to check this model and also to confirm the lead nonstoichiometry a structural study of the lead deficient phase $Pb_{0.8}Sr_4Fe_2O_{9-\delta}$ was undertaken.

The HREM study of different microcrystals of this phase shows that the layer stacking along **c** (Fig. 1b), taking into account previous results for layered superconductors, corresponds to the sequence "Fe–Sr–Sr–Fe–Sr–Pb–Sr." Indeed, the double and triple rows of bright dots which are stacked along **c** alternately can be correlated with two adjacent $[SrO]_\infty$ layers (labeled S) and with one $(PbO)_\infty$ layer (labeled P) sandwiched between two $[SrO]_\infty$ layers, respectively. The single rows of weak spots which are interleaved between one double and one triple row of bright dots can be correlated with $[FeO_2]_\infty$ layers (labeled F). Therefore the ideal structure of the stoichiometric phase $PbSr_4Fe_2O_9$ (Fig. 2) consists of the stacking of single octahedral perovskite layers $[SrFeO_3]_\infty$ with single rock salt layers $[SrO]_\infty$ and double rock salt layers $[(SrO)(PbO)]_\infty$ alternately, keeping in mind that the stacking of two SrO layers form a single rock salt layer and that the sequence of three layers "SrO–PbO–SrO" forms a double rock salt layer. Thus this structure obeys a mechanism similar to that observed for the thallium cuprate $TlBa_{2-x}La_{2+x}Cu_2O_{9\pm\delta}$ (*19*); i.e., it can be described as the intergrowth of 1201-$[PbSr_2FeO_5]_\infty$-type layers with 0201-$[Sr_2FeO_4]_\infty$-type layers. However, for $x = 0.2$, a significant lead deficiency in the rock salt layer should appear, as well as oxygen vacancies which can be distributed either in the rock salt or in the perovskite layers.

Based on the HREM study, powder X-ray structure calculations were performed for $x = 0.2$ in order to check the

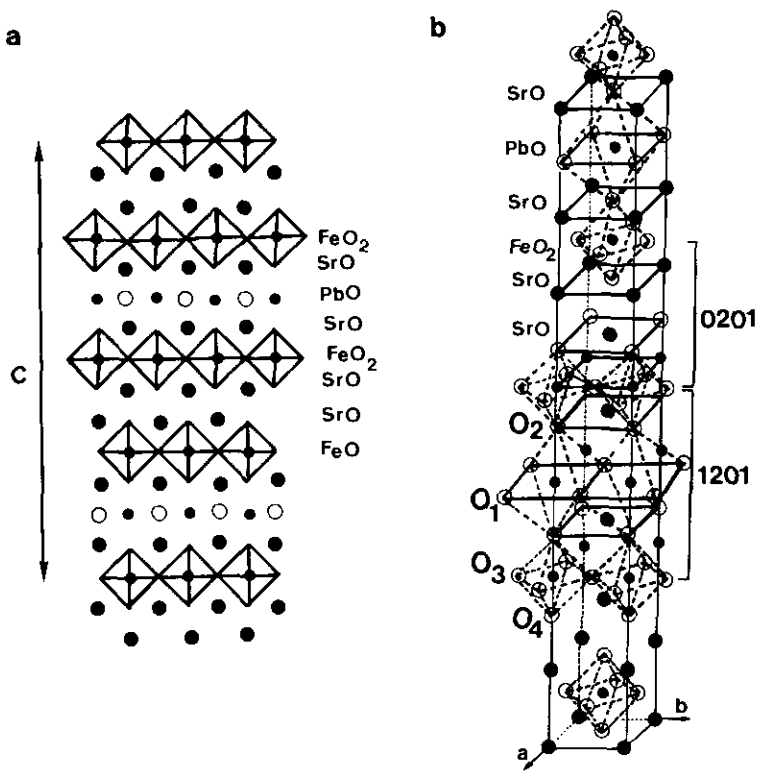

FIG. 2. Schematic representation of the ideal crystallographic structure of $PbSr_4Fe_2O_9$ built up from the regular intergrowth of 0201-$[Sr_2FeO_4]$ and 1201-$[PbSr_2FeO_5]$ structural units: (a) projected along a; (b) perspective view.

lead nonstoichiometry and the validity of the structural model. The refinements were carried out in the I_4/mmm space group with initial locations of the atoms corresponding to those reported for $TlBa_{2-x}La_{2+x}Cu_2O_{9\pm\delta}$ (*19*). As the structure includes heavy ions like Pb and Sr, it would be unreasonable from X-ray powder data to attempt to refine the occupancy factors of the oxygens which were arbitrarily fixed to 1. However, because of the probable existence of a lead deficiency of the samples, oxygen vacancies should be present on O sites.

The first step of the refinement leads to a reliability factor calculated on the intensities $R_I = \Sigma|I_o - I_c|/\Sigma I_o$ close to 0.117. The refinement for Pb yields an isotropic temperature factor of 3.8 Å^2 and an occupancy of 0.80 in good agreement with the chemical data.

Because of the relatively high value of R_I, subsequent refinements were then attempted in order to lower it. First, we considered a splitting of the Pb site, i.e., 2(*a*) (0, 0, 0) to 8(*i*) (x, 0, 0), which allows us to decrease the thermal factor to 2.1 Å^2 without a change of R_I. In contrast, the R value is significantly lowered to 0.085 by splitting the O(2) sites which correspond to the apical vertices common to the PbO_6 and FeO_6 octahedra. Refined atomic coordinates are summarized in Table II. The observed and calculated XRD patterns obtained by Rietveld analysis, together with their difference (Fig.

TABLE II

ATOMIC COORDINATES CALCULATED FOR $Pb_{1-x}Sr_4Fe_2O_{9-\delta}$ ($x \approx 0.2$) AT 298 K

Atom	Site symmetry	x	y	z	B (Å^2)	Unit cell occupancy
Pb	8*i*	0.060(4)	0	0	2.4(2)	1.57(3)
Sr(1)	4*e*	0.5	0.5	0.0851(1)	1.0(1)	4.
Sr(2)	4*e*	0.5	0.5	0.2054(1)	1.0(1)	4.
Fe	4*e*	0	0	0.1499(2)	1.5(1)	4.
O(1)	2*b*	0	0	0.5	2.	2.
O(2)	16*n*	0.192(8)	0	0.0694(4)	2.	4.
O(3)	8*g*	0.5	0	0.1441(6)	2.	8.
O(4)	4*e*	0	0	0.2124(3)	2.	4.

Note. e.s.d.'s are given in parentheses.

3), attest to the validity of the structural model given in Fig. 2. The refinements confirm the existence of a lead deficiency without ambiguity. The interatomic distances (Table III) are in agreement with those usually observed in oxides. Namely the Sr(2)–O distances, ranging from 2.52 to 2.72 Å, are similar to those observed for Sr_2FeO_4 (*20*). The shortest Pb–O distances of 2.19 Å are those usually observed for Pb(IV). The four Fe–O equatorial distances of the $[FeO_2]_\infty$ layers, i.e., corresponding to the basal plane of the FeO_6 octahedra, of 1.926 Å are similar to those observed in Sr_2FeO_4; in contrast the apical Fe–O distances, involving a short bond (Fe–O(4) = 1.916 Å) and an abnormally long bond (Fe–O(2) = 2.57 Å), show that iron exhibits, in fact, a pyramidal coordination. This coordination of Fe(III) is in agreement with the ability of iron to occupy

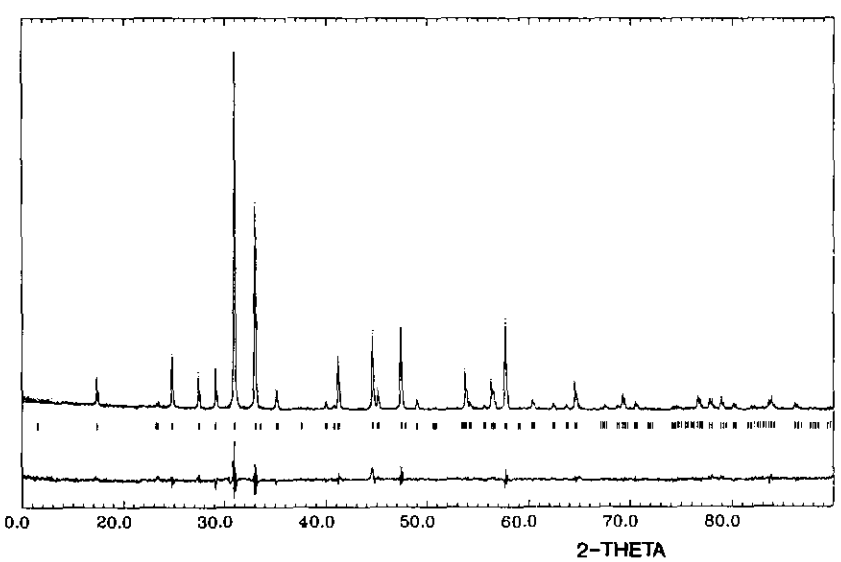

FIG. 3. Final profile fit and difference pattern for the XRD data for $Pb_{1-x}Sr_4FeO_{9-\delta}$ ($x \approx 0.2$).

TABLE III

CALCULATED INTERATOMIC DISTANCES WITH e.s.d's IN PARENTHESES

Atoms	Distances (Å)	Atoms	Distances (Å)
Pb–O(1)	2.55(1) × 2	Fe–O(3)	1.926(2) × 4
Pb–O(1)	2.88(1) × 2	Fe–O(4)	1.916(6) × 1
Pb–O(2)	2.19(1) × 2	Fe–O(2)	2.57(1) × 1
Sr(1)–O(2)	2.30(2) × 4	Sr(2)–O(3)	2.68(1) × 4
Sr(1)–O(3)	2.64(1) × 4	Sr(2)–O(4)	2.720(1) × 4
Sr(1)–O(1)	2.609(3) × 1	Sr(2)–O(4)	2.520(3) × 1

the pyramidal sites of the $YBa_2Cu_3O_7$ (*1–6*) and $YBaFeCuO_5$ (*21*) structures.

These results confirm definitely that $Pb_{1-x}Sr_2Fe_2O_{9-\delta}$ is isostructural with $TlBa_{2-x}La_{2+x}Cu_2O_{9\pm\delta}$ (*19*); i.e., it corresponds to a regular intergrowth of the 1201 and 0201 structures corresponding to $[Pb_{1-x}Sr_2FeO_{5-\delta}]_\infty$ and $[Sr_2FeO_4]_\infty$ layers, respectively. Nevertheless, it must be pointed out that the $R_{(I)}$ factor remains rather high. In order to understand such a feature a systematic observation of numerous crystals by HREM has been undertaken. It reveals that in a great number of them the contrast is often disturbed because of the existence of order–disorder phenomena and stacking faults. Two typical examples of disturbed contrast are shown in Figs. 4a and 4b. In the first image (Fig. 4a) the variations in size and brightness of the white dots correlated with the zones of low electron density concern only short segments of one or two adjacent layers; some areas are pointed out with curved arrows. These variations suggest local changes in the ion nature correlated with displacements of the atoms. The through-focus series of the images show that the cationic and anionic lattices are both affected by these features. In the second example (Fig. 4b), the amplitude of the phenomenon is more important in size as well as in intensity so that the nature of the layers is no longer obvious. Such features often involve undulations of the atomic layers; in some crystals, they are so strong and the matrix so distorted that they prevent any direct interpretation of the contrast.

A second important structural feature must be described, dealing with the existence of stacking defects which are generally observed in the form of outgrowth on the crystal edges. An example is shown in Fig. 5. In this part of the crystal, the contrast consists of double rows of white dots correlated with the $[SrO]_\infty$ layers, separated by three or five rows of alternating weak and bright dots correlated with the $[FeO_2]_\infty$ and $[SrO]_\infty$ layers, respectively. In this way, the local structure can be interpreted as an intergrowth of single rock salt layers with double and triple perovskite layers leading to the formation of "0212" slices ($Sr_3Fe_2O_{7-\delta}$) and "0223" slices ($Sr_4Fe_3O_{10-\delta}$) (Fig. 6). In this crystal, the 0212 slices are more numerous; one is marked, as an example, with a black triangle, whereas the 0223 slices are marked with curved arrows. The close relationships between the parent structure, [1201/0201], and the 0223 defective slices must be outlined. The 0223 structure can indeed be described from the replacement of a $[PbO]_\infty$ layer by a $[FeO_2]_\infty$ layer; in such a replacement, a double rock salt layer is substituted by a perovskite layer, involving a strong shortening of the c parameter ($c/2$ varying from 15.3 to 14 Å) but retaining the *I*-type symmetry (Fig. 7). These substitu-

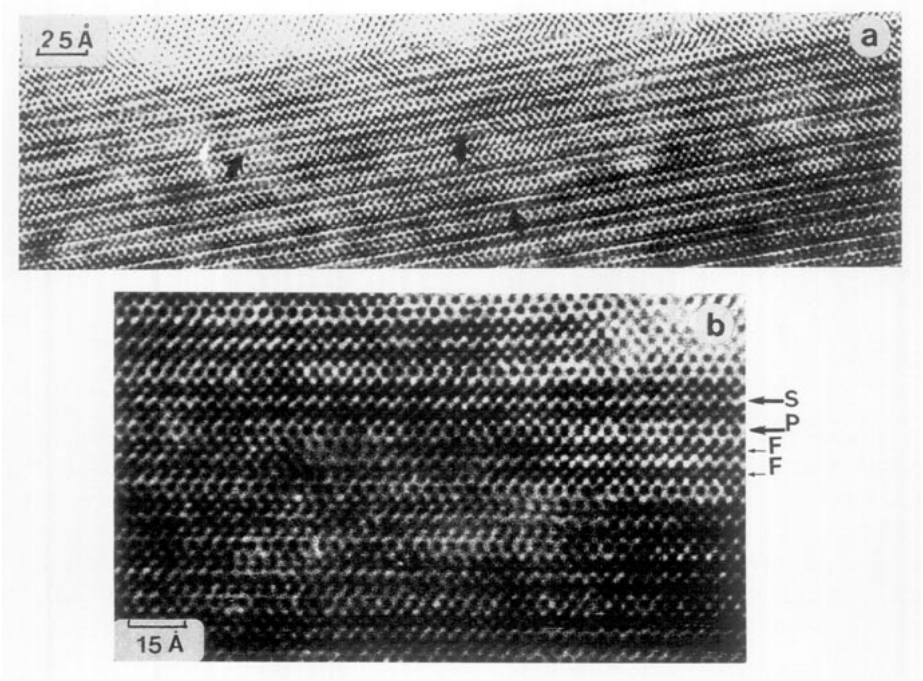

FIG. 4. (a) Overall [100] image showing local variation of the contrast. Rock salt and perovskite layers are both hit. (b) Enlarged image of an area where the contrast is highly disturbed. The nature of the layer is no longer evident. Note the crystal edge, wrapped in a SrO film.

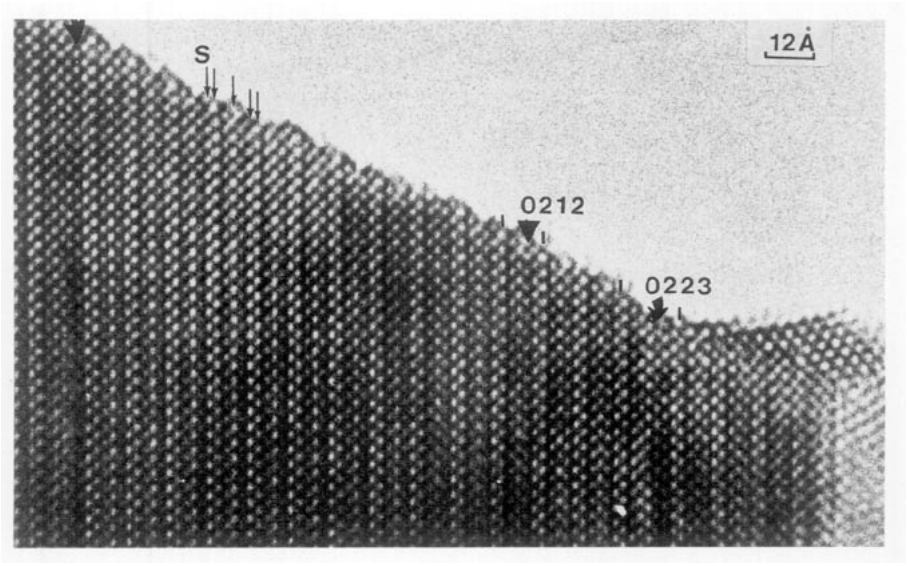

FIG. 5. [100] image of a defective area where "0212" and "0223" members are intergrown. The $[SrO]_x$ layers appear as rows of bright dots (small arrows).

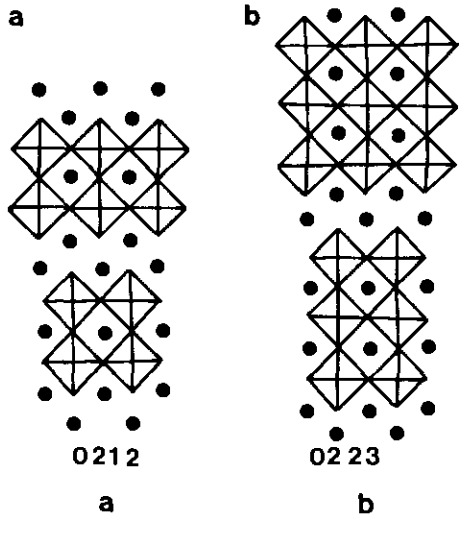

FIG. 6. Idealized models of "0212" and "0223" members built up, respectively, from the intergrowth of (a) a single rock salt layer and a double perovskite layer, and (b) a single rock salt layer and a triple perovskite layer.

tions are indeed easily interpreted in the outgrowth part of the crystal, where no distortions of the matrix are involved by such structural phenomena; in the [1201/0201] matrix, the existence of similar features cannot be ruled out in the disturbed and distorted part of the crystals, where the contrast cannot be simply interpreted. Last, it must be pointed out that in numerous crystals, the edge is wrapped by a film some 10 Å thick; it can be observed at the top of Fig. 4a and in the left part of Fig. 5. The contrast and interatomic distances at that level are consistent with a SrO composition of the extra layers. Note that the junction between the different layers is perfectly coherent and

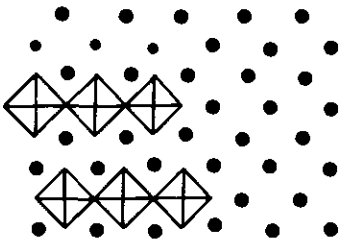

FIG. 8. Idealized drawing showing the easy connection between [SrO] and perovskite layers.

that the $[FeO_2]_\infty$ layers of the perovskite slabs are simply replaced by $[SrO]_\infty$ layers; this is clearly observed at the right top of Fig. 4b and the schematic model is drawn in Fig. 8.

Mössbauer spectroscopy and magnetic susceptibility measurements. Title compounds corresponding to different x values ($0 \leq x \leq 0.2$) were characterized by Mössbauer spectrscopy. As shown in Fig. 9, the RT Mössbauer spectra of the compounds exhibit a doublet with broadened and asymmetrical lines which indicate the presence of pure electric quadrupolar interactions. The isomer shift values (see Table IV) of the iron sites show that iron is always trivalent whatever x may be. One observes two iron sites for $x = 0$, i.e., for $PbSr_4Fe_2O_9$, while three iron sites must be taken into account for x differing from zero, i.e., for lead-deficient oxides. It is worth pointing out from Table IV that the percentage of the first site (ΔQ = 0.81–0.83 mm/sec) remains rather constant while that of site 2 (ΔQ = 0.63–0.69 mm/sec) increases as the lead content increases, contrary to the percentage of the site 3 (ΔQ = 0.31–0.46 mm/sec) which decreases.

FIG. 7. Compared idealized drawing of double rock salt layers and single perovskite layers. They differ only in the nature of the intermediate layers which are $[AO]_\infty$ and $[FeO_2]_\infty$, respectively.

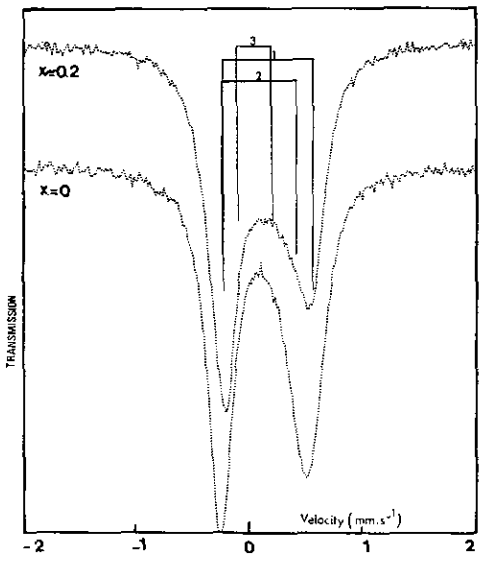

FIG. 9. Mössbauer spectra of $Pb_{1-x}Sr_4Fe_2O_{9-\delta}$ at 300 K with $x \approx 0.2$ and $x = 0$. The quadrupole doublets indicated by vertical lines 1, 2, and 3 correspond to Fe^{3+} species specified in Table IV.

Note also that the third site corresponds to quadrupole splittings which involve a more regular environment of Fe^{3+} ions than the other two which correspond to high quadrupole splittings. As a result, one may assume, because of the Pb-ion deficiency ($x \neq 0$), that the third site comes from a shift of the oxygen O(2) toward an upper position near the iron site, such a shift of O(2) being connected with a Pb-ion vacancy in the (Pb–O) plane. Concomitantly, the existence of oxygen vacancies on the O sites would be responsible for the appearance of $[FeO_5]$ pyramids in addition to highly distorted $[FeO_6]$ octahedra. One can thus explain the three iron sites needed to fit the Mössbauer spectra of the lead-deficient oxides but also the fact that the percentage of the third site increases as x increases. For $x = 0$, two iron sites have to be considered, both being characterized by wide quadrupole splittings (Table IV). The latter sites correspond to highly distorted FeO_6 octahedra, i.e., to a 5 + 1 coordination of iron which can result from the oxygen location (O(2) site) in the

TABLE IV

MÖSSBAUER PARAMETERS AT ROOM TEMPERATURE FOR $Pb_{1-x}Sr_4Fe_2O_{9-\delta}$ COMPOUNDS

Lead content[a] ±0.05	IS(mm · sec^{-1}) ±0.01	Γ(mm · sec^{-1}) ±0.01	ΔQ(mm · sec^{-1}) ±0.02	% ±5	Site
0.82	0.27	0.25	0.81	39	1
	0.19	0.30	0.67	31	2
	0.14	0.39	0.31	30	3
0.89	0.27	0.24	0.83	33	1
	0.20	0.30	0.69	33	2
	0.16	0.42	0.35	34	3
0.94	0.27	0.24	0.82	34	1
	0.22	0.36	0.63	56	2
	0.06	0.23	0.46	10	3
1.0	0.27	0.22	0.82	29	1
	0.22	0.34	0.69	71	2

Note. IS, isomer shift relative to metallic iron; Γ, half-height width; ΔQ, quadrupole splitting; %, fitted intensity of different sites.

[a] The lead content reported here corresponds to that deduced from oxidometric titrations. For more details see Table I.

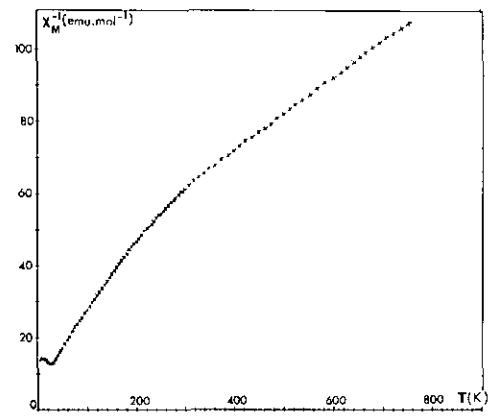

FIG. 10. Temperature dependence of the reciprocal magnetic susceptibility for $Pb_{1-x}Sr_4Fe_2O_{9-\delta}$ with $x \approx 0.2$.

Sr–O(2) plane in agreement with the X-ray analysis.

The evolution of the reciprocal magnetic susceptibility versus temperature for $x \approx 0.2$ (Fig. 10) shows the presence of a minimum near $T \approx 30$ K, characteristic of a two-dimensional antiferromagnetic behavior. The experimental value of μ_{eff} (6.3 μB) deduced from the Curie–Weiss domain above 340 K is slightly higher than the theoretical value of high spin Fe^{3+} ($\mu_{eff} = 5.9$ μB).

Concluding Remarks

These results show the ability of iron to form layered structures isotypic with those observed for superconductive cuprates. The HREM observations show, like for lead cuprates, an inhomogeneous distribution of cations, anions, and vacancies, and sometimes a strong distortion of the matrix; moreover, the intergrowth defects observed here suggest that the synthesis of other layered structures involving regular intergrowths of single and double rock salt layers with triple or quadruple iron layers should be investigated. The 5 + 1 and pyramidal coordinations of iron deduced from the Mössbauer spectroscopy are in agreement with XRD results. A neutron diffraction study of this phase should be performed in order to understand the real arrangement of oxygen atoms especially at the level of the rock salt layers.

References

1. G. XIAO, F. H. STREITZ, A. GAVRIN, Y. W. DU, AND C. L. CHIEN, *Phys. Rev. B* **35,** 8782 (1987).
2. J. M. TARASCON, P. BARBOUX, P. F. MICELI, L. H. GREENE, G. W. HULL, M. EIBSCHUTZ, AND S. A. SUNSHINE, *Phys. Rev. B* **37** (1988).
3. G. ROTH, G. HEGER, B. RENKER, J. PANNETIER, V. CAIGNAERT, M. HERVIEU, AND B. RAVEAU, *Z. Phys.* **71,** 43 (1988).
4. P. BORDET, J. L. HODEAU, P. STROBEL, M. MAREZIO, A. SANTORO, C. CHAILLOUT, AND J. J. CAPPONNI, *Physica C* **153–155,** 582 (1988).
5. M. HENNION, I. MIREBEAU, G. CODDENS, A. MENELLE, T. E. PHILLIPS, K. MOORJANI, AND M. HERVIEU, *Physica C* **159,** 124 (1989).
6. E. SUARD, V. CAIGNAERT, A. MAIGNAN, AND B. RAVEAU, *Physica C* **182,** 219 (1991).
7. M. HERVIEU, C. MICHEL, N. NGUYEN, R. RETOUX, AND B. RAVEAU, *Eur. J. Solid State Inorg. Chem.* **25,** 375 (1988).
8. R. RETOUX, C. MICHEL, M. HERVIEU, N. NGUYEN, AND B. RAVEAU, *Solid State Commun.* **69,** 599 (1989).
9. M. A. SUBRAMANIAN, J. GOPALAKRISHNAN, C. C. TORARDI, P. L. GAI, E. D. BOYES, T. R. ASKEW, R. B. FLIPPEN, W. E. FARNETH, AND A. W. SLEIGHT, *Physica C* **157,** 124 (1989).
10. J. Y. LEE, J. S. SWINNEA, AND H. STEINFINK, *J. Mater. Res.* **4,** 763 (1989).
11. T. MAEDA, K. SAKUYAMA, S. KORIYAMA, H. YAMAUCHI, AND S. TANAKA, *Phys. Rev. B* **43,** 7866 (1991).
12. X. X. TANG, D. E. MORRIS, AND A. P. B. SINKA, *Phys. Rev. B* **43,** 7936 (1991).
13. M. KOSUGE, T. MAEDA, K. SAKUYAMA, H. YAMAUCHI, N. KOSHIZUKA, AND TANAKA, *Physica C* **182,** 157 (1991).
14. A. MAIGNAN, T. ROUILLON, D. GROULT, J. PROVOST, M. HERVIEU, C. MICHEL, B. RAVEAU, R. S. LIU, AND P. P. EDWARDS, *Physica C* **177,** 461 (1991).
15. T. ROUILLON, J. PROVOST, M. HERVIEU, D. GROULT, C. MICHEL, AND B. RAVEAU, *Physica C* **159,** 201 (1989); *J. Solid State Chem.* **84,** 375 (1990).
16. T. ROUILLON, A. MAIGNAN, M. HERVIEU, C. MICHEL, D. GROULT, AND B. RAVEAU, *Physica C* **171,** 7 (1990).

17. M. Huvé, C. Michel, C. Martin, M. Hervieu, A. Maignan, J. Provost, and B. Raveau, *Physica C* **179,** 214 (1991).
18. D. B. Wiles and R. A. Young, *J. Appl. Crystallogr.* **14,** 149 (1981).
19. C. Martin, A. Maignan, M. Huvé, M. Hervieu, C. Michel, and B. Raveau, *Physica C* **179,** 1 (1991).
20. S. E. Dann, M. T. Weller, and D. B. Currie, *J. Solid State Chem.* **92,** 237 (1991).
21. L. Er-Rakho, C. Michel, and B. Raveau, *J. Solid State Chem.* **73,** 531 (1988).